The extraordinary structural evolution of massive galaxies

Szomoru, D.

CHAPTER 4

SIZES AND SURFACE BRIGHTNESS PROFILES OF QUIESCENT GALAXIES AT Z $\sim$ 2

We use deep *Hubble Space Telescope* Wide Field Camera 3 near-infrared imaging obtained of the GOODS-South field as part of the CANDELS survey to investigate a stellar mass-limited sample of quiescent galaxies at $1.5 < z < 2.5$. We measure surface brightness profiles for these galaxies using a method that properly measures low surface brightness flux at large radii. We find that quiescent galaxies at $z \sim 2$ very closely follow Sérsic profiles, with $n_{median} = 3.7$, and have no excess flux at large radii. Their effective radii are a factor ~ 4 smaller than those of low-redshift quiescent galaxies of similar mass. However, there is significant spread in sizes ($\sigma_{\log_{10} r_e} = 0.24$), with the largest $z \sim 2$ galaxies lying close to the $z = 0$ mass-size relation. We compare the stellar mass surface density profiles with those of massive elliptical galaxies in the Virgo cluster and confirm that most of the mass-growth which occurs between $z \sim 2$ and $z = 0$ must be due to accretion of material onto the outer regions of the galaxies. Additionally, we investigate the evolution in the size distribution of massive quiescent galaxies. We find that the minimum size growth required for $z \sim 2$ quiescent galaxies to fall within the $z = 0$ size distribution is a factor ~ 2 smaller than the total median size growth between $z \sim 2$ and $z = 0$.

Daniel Szomoru, Marijn Franx, Pieter G. van Dokkum
The Astrophysical Journal, **749**, 121-131, 2012

4.1 INTRODUCTION

Quiescent galaxies make up a considerable fraction of the massive galaxy population at $z = 2$ (e.g., Franx et al. 2003; Daddi et al. 2005; Kriek et al. 2006). Their structural evolution has been the subject of considerable discussion, focusing in particular on their extremely compact nature compared to low redshift galaxies of similar mass (e.g., Daddi et al. 2005; Trujillo et al. 2006; Toft et al. 2007; van der Wel et al. 2008; van Dokkum et al. 2008; Damjanov et al. 2009; Hopkins et al. 2009; Saracco et al. 2009; van Dokkum et al. 2009; Cassata et al. 2010; Mancini et al. 2010; Cassata et al. 2011). The early formation and subsequent evolution of these massive, compact objects presents a considerable challenge to current models of galaxy formation and evolution (e.g., Wuyts et al. 2010; Oser et al. 2012). It is unclear what the structure of the progenitors of these galaxies is, and the lack of extremely compact massive galaxies at low redshift implies considerable size evolution between $z = 2$ and $z = 0$ (Trujillo et al. 2009; Taylor et al. 2010). However, efforts to accurately quantify this evolution are hindered by uncertainties. The apparent compactness of $z \sim 2$ quiescent galaxies may simply be an observational effect: photometric masses may be systematically overestimated due to modeling uncertainties, and sizes may be underestimated due to a lack of imaging depth (Hopkins et al. 2009; Muzzin et al. 2009).

Due to the difficulty of obtaining high-quality spectra of quiescent galaxies at $z > 1.5$, dynamical masses have only been measured for a few such galaxies (Cappellari et al. 2009; Cenarro & Trujillo 2009; van Dokkum et al. 2009; Onodera et al. 2010; van de Sande et al. 2011). Instead, photometric stellar masses are used, which are subject to considerable uncertainties due to e.g., the quality of the stellar libraries used in modeling the spectral energy distribution (SED), or incorrect assumptions about the shape of the initial mass function (IMF). These uncertainties can result in systematic errors of up to a factor ~ 6 (Conroy et al., 2009). At low redshift there is good agreement between stellar masses determined by photometric SED fitting methods and dynamical masses (Taylor et al. 2010). Whether this is also the case at high redshift is unclear (e.g., van de Sande et al. 2011; Bezanson et al. 2011; Martinez-Manso et al. 2011).

The second large source of uncertainty lies in the size determination of these galaxies. The compact objects observed at $z \sim 2$ may be surrounded by faint extended envelopes of material, which could be undetected by all but the deepest data. Stacking studies have been used to obtain constraints on the average surface brightness profile of compact galaxies (e.g., van der Wel et al. 2008; van Dokkum et al. 2008; Cassata et al. 2010). However, detailed analysis of individual galaxies is more difficult, primarily due to the limited number of compact galaxies for which ultradeep near-infrared (NIR) data are available. Szomoru et al. (2010) carried out an analysis on a $z = 1.91$ compact quiescent galaxy in the Hubble Ultra Deep Field (HUDF) and confirmed its small size.

In this Paper we expand the analysis of Szomoru et al. (2010) using a stellar mass-limited sample of 21 quiescent galaxies. We make use of deep *Hubble Space Telescope* Wide Field Camera 3 (*HST* WFC3) data from the CANDELS GOODS-South observations to investigate the surface brightness profiles of quiescent galaxies at $z \sim 2$. These observations

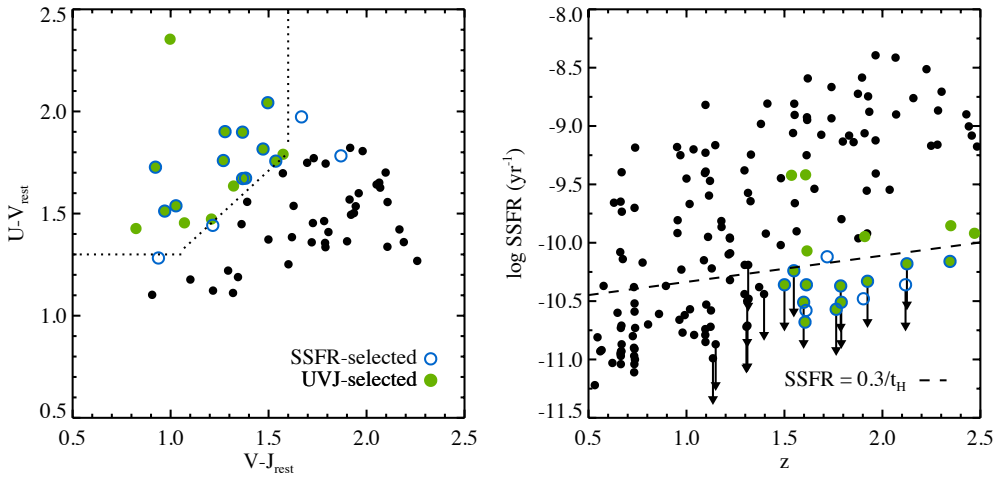

Figure 4.1: Left panel: rest-frame $U-V$ and $V-J$ colors of galaxies in the CANDELS GOODS-South deep field at $1.5 < z < 2.5$. Right panel: specific star formation rates as a function of redshift. Arrows indicate upper limits. The dashed line indicates where the specific star formation rate is equal to $0.3/t_H$. Quiescent galaxies selected using the UVJ color criterion are shown as filled green circles. Galaxies which are selected as quiescent based on their SSFRs are shown as open blue circles. There is good agreement between the two selection criteria. Both the UVJ-selected galaxies and the SSFR-selected galaxies are included in our quiescent galaxy sample.

are not as deep as the HUDF data, but cover a much larger area, allowing us to study a statistically more meaningful sample. We measure the surface brightness profile of each individual galaxy and investigate deviations from Sérsic profiles. Additionally, we compare the size distribution and profile shapes of $z \sim 2$ galaxies to those of low redshift quiescent galaxies. Throughout the Paper, we assume a ΛCDM cosmology with $\Omega_m = 0.3$, $\Omega_\Lambda = 0.7$ and $H_0 = 70$ km s^{-1} Mpc^{-1}. All stellar masses are derived assuming a Kroupa IMF (Kroupa, 2001). All effective radii are circularized and magnitudes are in the AB system.

4.2 DATA AND SAMPLE SELECTION

We use NIR data taken with *HST* WFC3 as part of the CANDELS survey (Grogin et al. 2011; Koekemoer et al. 2011). This survey will target approximately 700 square arcminutes to 2 orbit depth in Y_{105}, J_{125} and H_{160} (COSMOS, EGS and UDS fields), as well as $\sim$ 120 square arcminutes to 12 orbit depth (GOODS-South and GOODS-North fields). These NIR observations are complemented with parallel *HST* ACS exposures in V_{606} and I_{814}. We use the deepest publicly available data, reduced by Koekemoer et al. (2011), which consist of I_{814}, J_{125} and H_{160} observations to 4-orbit depth of a $\sim$ 60 square arcminute section of the GOODS-South field. The full width at half-maximum of the point-spread function (PSF) is $\approx$ 0.18 arcsec for the WFC3 observations and $\approx$ 0.11 arcsec for the ACS

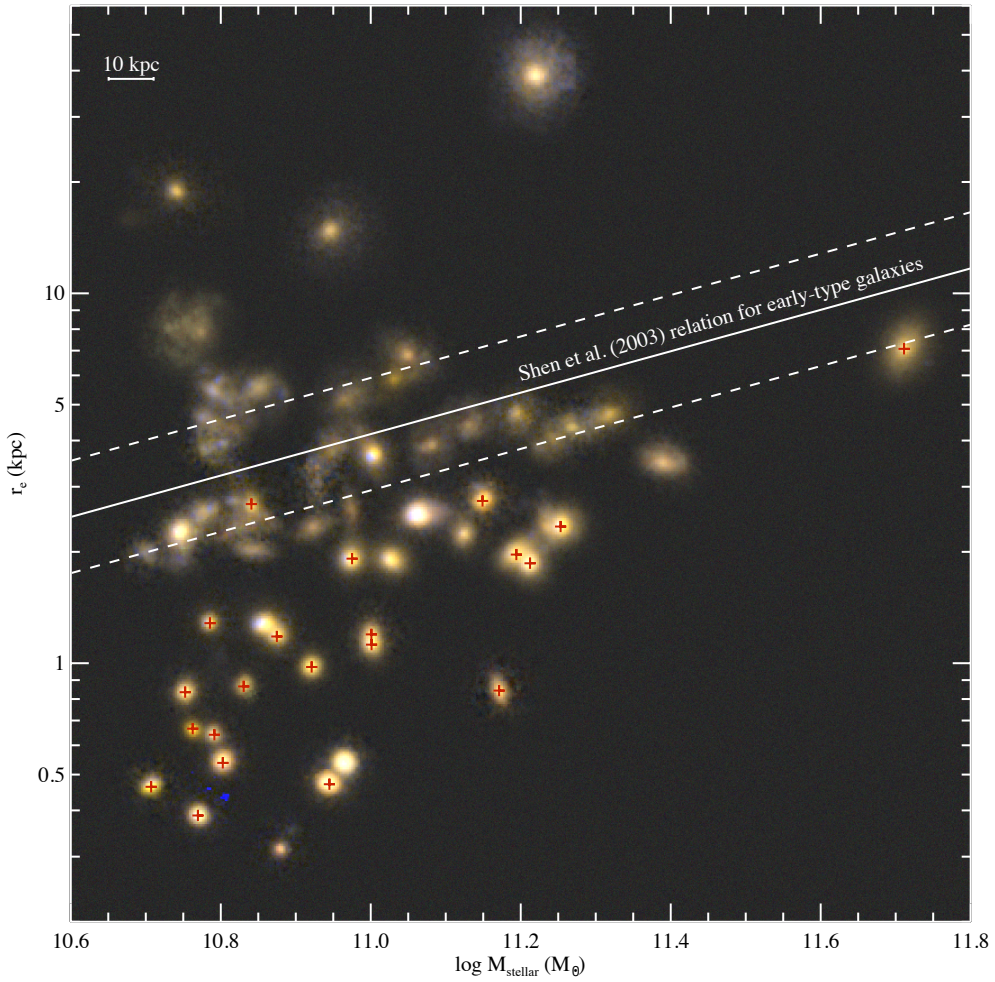

Figure 4.2: Stellar masses and sizes of galaxies at $1.5 < z < 2.5$ with $M_{stellar} > 5 \times 10^{10} M_{\odot}$. Color images are composed of rest-frame U_{336}, B_{438} and g_{475} images, obtained from observed I_{814}, J_{125} and H_{160} images. Galaxies which are included in our quiescent sample are indicated with red crosses. Although we do not select based on morphology, almost all galaxies in our quiescent sample are compact, bulge-dominated, and have red colors.

observations. The images have been drizzled to a pixel size of 0.06 arcsec for the WFC3 observations and 0.03 arcsec for the ACS observations (see Koekemoer et al. (2011) for details).

Galaxies are selected in the GOODS-South field using the K_s-selected FIREWORKS catalog (Wuyts et al., 2008). This catalog combines observations of the Chandra Deep Field South ranging from ground-based U-band data to *Spitzer* 24 μm data, and includes spectroscopic redshifts where available, as well as photometric redshifts derived using EAZY (Brammer et al., 2008). These photometric redshifts have a median $\Delta z/(1+z) = -0.001$ with a normalized median absolute deviation of $\sigma_{\rm NMAD} = 0.032$ (Wuyts et al., 2008). Stellar masses were estimated from SED fits to the full photometric data set (N. M. Förster Schreiber et al. 2012, in preparation), assuming a Kroupa IMF and the stellar population models of Bruzual & Charlot (2003).

We select all galaxies with $1.5 < z < 2.5$ and stellar masses above $5 \times 10^{10} M_{\odot}$, which is the completeness limit in this redshift range (Wuyts et al., 2009). In order to ensure that we include all quiescent galaxies we explore both a color-color selection (the UVJ selection described in Williams et al. (2009)) and a selection based on specific star formation rate (SSFR). In the left panel of Figure 4.1 we show the rest-frame $U-V$ and $V-J$ colors of all $z \sim 2$ galaxies in the field. The dashed lines indicate the quiescent galaxy selection limits from Williams et al. (2009). Galaxies which fall within the dashed lines (green dots) have SEDs that are consistent with red, quiescent galaxies. Patel et al. (2012) have shown that this selection method is very effective at separating dust-reddened starforming galaxies from truly quiescent galaxies. As an alternative to the UVJ selection we also select galaxies based on their SSFR. In the right-hand panel of Figure 4.1 we show the SSFRs of galaxies as a function of redshift. The SSFRs are estimated from the UV and 24 μm fluxes, as discussed in Wuyts et al. (2009). The dashed line shows our selection limit, below which the SSFR is lower than $0.3/t_H$, where t_H is the Hubble time. There is generally very good agreement between the two selection criteria, although several galaxies that seem to be quiescent based on their SSFRs are not selected by the UVJ method, and vice versa. We find no significant difference in the distribution of structural parameters of galaxies selected by either method; the median values are equal to within 6 percent, for the effective radii, Sérsic indices and axis ratios. This is expected, given the large overlap between the two samples. Since we wish to be as complete as possible we combine the two selection methods and include all galaxies selected by either method. This results in a sample of 21 quiescent galaxies, whose properties are summarized in Table 4.1.

To illustrate the effects of our selection on galaxy morphology we show color images of all galaxies with $1.5 < z < 2.5$ and $M_{stellar} > 5 \times 10^{10} M_{\odot}$ in the stellar mass-size plane in Figure 4.2. The color images are constructed from PSF-matched rest-frame U_{336}, B_{438} and g_{475} images, obtained by interpolating between the observed I_{814}, J_{125} and H_{160} images. Although we do not select based on morphology, the galaxies in our quiescent sample (indicated with red crosses) are generally very compact, bulge-dominated systems with relatively red colors. Interestingly, all starforming systems at $z \sim 2$ appear to have a well-defined red core, as was also pointed out by Szomoru et al. (2011) (but also see, e.g.,

Förster Schreiber et al. 2011a; Förster Schreiber et al. 2011).

4.3 MEASURING SURFACE BRIGHTNESS PROFILES

Obtaining surface brightness profiles of high-redshift galaxies is difficult, in large part due to the small size of these galaxies compared to the PSF. Direct deconvolution of the observed images is subject to large uncertainties. A common approach is therefore to fit two-dimensional models, convolved with a PSF, to the observed images. Sérsic (1968) profiles are commonly used, since these have been shown to closely match the surface brightness profiles of nearby early-type galaxies (e.g., Caon et al. 1993; Graham et al. 2003; Trujillo et al. 2004; Ferrarese et al. 2006; Côté et al. 2007; Kormendy et al. 2009). However, there is no reason that high-redshift galaxies should exactly follow Sérsic profiles.

An obvious way to account for deviations from a Sérsic profile is by using double-component fits, in which the deviations are approximated by a second Sérsic profile. Although this provides a closer approximation to the true surface brightness profile than a one-component fit, it still depends on assumptions regarding the shape of the profile. We therefore use a technique which is more robust to deviations from the assumed model and accurately recovers the true intrinsic profile. This technique was first used in Szomoru et al. (2010); we summarize it here. First, we use the GALFIT package (Peng et al., 2002) to perform a conventional two-dimensional Sérsic profile fit to the observed image. For PSFs we use unsaturated stars brighter than $K = 22.86$ that are not contaminated by nearby sources. We verify the quality of our stellar PSFs by comparing their radial profiles to each other, and find that the profiles show small variations in half-light radius of order $\sim 2\%$. We find no systematic dependence of these variations with magnitude. In order to estimate the effects of PSF variations on our derived parameters we fit every galaxy using each of the stars separately. We find that the derived total magnitudes, sizes and Sérsic indices vary by about 0.1%, 3% and 7%, respectively.

After fitting a Sérsic model profile we measure the residual flux profile from the residual image, which is the difference between the observed image and the best-fit PSF-convolved model. This is done along concentric ellipses which follow the geometry of the best-fit Sérsic model. The residual flux profile is then added to the best-fit Sérsic profile, effectively providing a first-order correction to the profile at those locations where the assumed model does not accurately describe the data. The effective radius is then calculated by integrating the residual-corrected profile out to a radius of approximately 12 arcseconds ($\sim$ 100 kpc at $z \sim 2$). We note that the residual flux profile is not deconvolved for PSF; however, we show below that this does not strongly affect the accuracy of this method.

Errors in the sky background estimate are the dominant source of uncertainty when deriving surface brightness profiles of faint galaxies to large radii. Using the wrong sky value can result in systematic effects. GALFIT provides an estimate of the sky background during fitting. To ensure that this estimate is correct we inspect the residual flux profile of each galaxy at radii between 5 and 15 arcsec (approximately 40 to 120 kpc at $z = 2$). Using

Table 4.1: Galaxy properties.

ID[a]	z	R.A	Dec	M_*^b ($\log M_\odot$)	SSFR ($\log \mathrm{yr}^{-1}$)	U-V$_{\rm rest}$	V-J$_{\rm rest}$	mag$^c_{H,app}$ (AB)	r_e^c (kpc)	n^c	b/a	P.A.[d] (deg)
1060	2.345*	53.069829	-27.880467	11.14	-10.16	1.75	0.92	22.21 ± 0.05	2.75 ± 1.60	9.21 ± 1.10	0.70 ± 0.01	-45.2 ± 1.6
1088	1.752*	53.065570	-27.878805	10.75	-10.12	1.28	0.94	21.84 ± 0.03	0.83 ± 0.11	5.50 ± 0.67	0.87 ± 0.02	-62.5 ± 13.1
1289	1.759*	53.116186	-27.871904	11.00	-10.51	2.04	1.50	22.35 ± 0.02	1.20 ± 0.22	3.26 ± 0.40	0.58 ± 0.01	-8.5 ± 0.8
1831	1.536	53.076366	-27.848700	11.25	-9.42	1.47	1.21	20.71 ± 0.02	2.34 ± 0.33	3.68 ± 0.16	0.92 ± 0.01	-44.6 ± 3.2
1971	1.608	53.150661	-27.843604	10.84	-9.42	1.63	1.32	21.71 ± 0.03	2.69 ± 0.79	5.07 ± 0.31	0.87 ± 0.01	27.0 ± 2.1
2227	1.612	53.150165	-27.834522	10.98	-10.36	1.54	1.03	21.40 ± 0.02	1.92 ± 0.26	3.76 ± 0.15	0.84 ± 0.01	-6.5 ± 2.1
2514	1.548*	53.151413	-27.825886	10.79	-10.24	1.67	1.38	21.96 ± 0.06	1.28 ± 0.29	5.73 ± 0.93	0.86 ± 0.03	7.0 ± 5.9
2531	1.598*	53.171735	-27.825672	10.87	-10.51	1.90	1.28	21.93 ± 0.02	1.18 ± 0.12	4.08 ± 0.30	0.95 ± 0.02	7.6 ± 11.6
2856	1.759*	53.216633	-27.814310	10.83	-10.37	1.76	1.54	22.90 ± 0.01	0.87 ± 0.03	1.20 ± 0.08	0.63 ± 0.02	-16.5 ± 1.0
2993	2.470	53.163233	-27.808962	10.71	-9.92	2.35	1.00	23.38 ± 0.02	0.46 ± 0.04	1.01 ± 0.09	0.32 ± 0.04	-63.1 ± 1.0
3046	2.125*	53.116519	-27.806731	10.80	-10.18	1.51	0.97	22.22 ± 0.02	0.54 ± 0.02	3.59 ± 0.34	0.70 ± 0.02	-45.8 ± 3.0
3119	2.349	53.123107	-27.803355	10.94	-9.85	1.43	0.82	21.97 ± 0.03	0.47 ± 0.06	5.09 ± 0.60	0.49 ± 0.04	79.2 ± 1.5
3242	1.910	53.158831	-27.797119	10.77	-9.95	1.45	1.07	22.10 ± 0.02	0.39 ± 0.03	4.17 ± 0.45	0.62 ± 0.03	57.1 ± 3.0
3548	1.500*	53.202356	-27.785436	10.76	-10.36	1.67	1.37	22.40 ± 0.03	0.67 ± 0.05	3.75 ± 0.48	0.65 ± 0.04	55.5 ± 2.4
3829	1.924*	53.069966	-27.768143	10.79	-10.33	1.90	1.37	22.85 ± 0.05	0.64 ± 0.14	4.24 ± 1.15	0.66 ± 0.03	44.7 ± 3.2
4850	2.118*	53.012891	-27.705730	11.17	-10.36	1.97	1.67	22.68 ± 0.02	0.84 ± 0.09	2.72 ± 0.42	0.20 ± 0.02	17.0 ± 0.3
5890	1.756*	53.174620	-27.753362	10.92	-10.57	1.76	1.27	22.09 ± 0.01	0.98 ± 0.04	1.89 ± 0.12	0.92 ± 0.02	-14.6 ± 3.6
6097	1.903	53.140997	-27.766706	11.21	-10.48	1.44	1.22	21.30 ± 0.03	1.86 ± 0.43	5.26 ± 0.56	0.79 ± 0.02	2.8 ± 2.2
6187	1.610	53.044923	-27.774363	11.71	-10.58	1.76	1.87	20.37 ± 0.01	7.08 ± 1.30	2.77 ± 0.05	0.61 ± 0.01	-30.1 ± 0.2
6194	1.605	53.052217	-27.774766	11.19	-10.68	1.82	1.47	21.18 ± 0.02	1.97 ± 0.14	2.04 ± 0.06	0.57 ± 0.01	-56.3 ± 0.4
6246	1.615	53.043813	-27.774666	11.00	-10.07	1.76	1.57	21.71 ± 0.03	1.12 ± 0.16	10.10 ± 2.38	0.64 ± 0.02	-19.6 ± 1.5

[a] FIREWORKS ID (Wuyts et al., 2008)

[b] Masses are corrected to account for the difference between the catalog magnitude and our measured magnitude.

[c] Magnitudes, effective radii and Sérsic indices are derived from the H_{160} band residual-corrected profiles discussed in Section 4.4.

[d] Position angles are measured counterclockwise with respect to North.

* No spectroscopic redshifts are available for these galaxies; photometric redshifts are listed instead

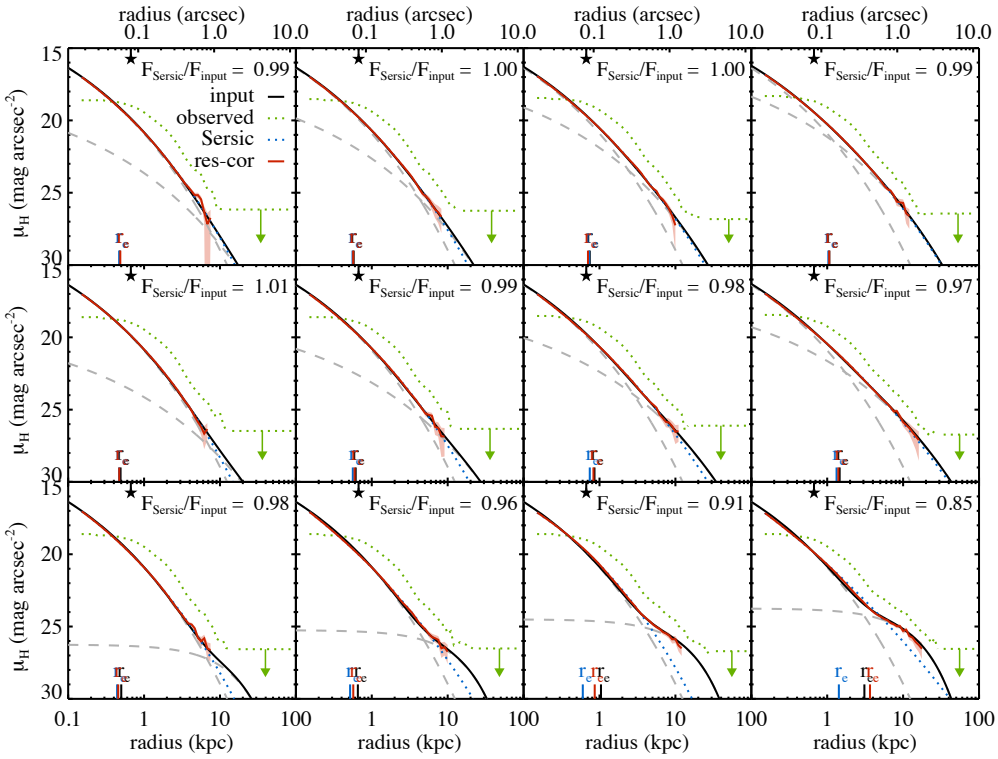

Figure 4.3: Effectiveness of the residual-correction for recovering surface brightness profiles. The method was tested on a large number of simulated galaxies, composed of two components: one compact bright component, and an extended fainter component. A small selection is shown here. The input profiles are shown in black, with the dashed grey lines indicating the two subcomponents. The PSF-convolved ``observed'' profiles are shown in green. Direct Sérsic fits are shown in blue, and the residual-corrected profiles are overplotted in red. The shaded light red regions indicate the 1-σ errors due to uncertainty in the sky estimation. The size of the PSF half width at half maximum (HWHM) is indicated on the top axis of each panel. Input effective radii are indicated in black on the bottom axes. Effective radii derived from the direct Sérsic fits and from the residual-corrected profiles are indicated in blue and red, respectively. The fraction of the input flux within 10 kpc recovered by the Sersic fits $F_{\rm Sersic}/F_{\rm input}$ is given in each panel. The residual-corrected profiles clearly reproduce the input profiles more accurately than the simple Sérsic fits, especially at large radii.

this portion of the residual flux profile we derive a new sky value and adjust the intensity profile accordingly. We use the difference between the minimum and maximum values of the residual flux profile within this range of radii as an estimate of the uncertainty in the sky determination.

In Szomoru et al. (2010) this procedure was tested using simulated galaxies inserted into *HST* WFC3 data of the HUDF. Since the data used in this Paper are shallower we have performed new tests. We create images of simulated galaxies that consist of two components: one compact elliptical component and a larger, fainter component that ranges from disk-like

Table 4.2: Surface brightness profiles.

ID[a]	$r_{\rm arcsec}$ (arcsec)	$r_{\rm kpc}$ (kpc)	μ_H (AB mag arcsec^{-2})	$\log \Sigma$ ($\log M_\odot$ kpc^{-2})
1060	0.0180	0.147	18.413 ± 0.0010	10.843 ± 0.0004
1060	0.0198	0.162	18.548 ± 0.0011	10.789 ± 0.0005
1060	0.0216	0.177	18.673 ± 0.0013	10.739 ± 0.0005
1060	0.0240	0.196	18.826 ± 0.0015	10.678 ± 0.0006
1060	0.0264	0.216	18.966 ± 0.0019	10.622 ± 0.0007
1060	0.0288	0.235	19.095 ± 0.0021	10.570 ± 0.0008
1060	0.0318	0.260	19.244 ± 0.0024	10.510 ± 0.0010
1060	0.0348	0.285	19.382 ± 0.0027	10.455 ± 0.0011
1060	0.0384	0.314	19.534 ± 0.0032	10.395 ± 0.0013
1060	0.0426	0.348	19.696 ± 0.0037	10.330 ± 0.0015
...	...	...	...	...

This is a sample of the full table, shown for illustrative purposes.
[a]FIREWORKS ID (Wuyts et al., 2008)

to elliptical. The axis ratio and position angle of the second component are varied, as are its effective radius and total magnitude. The simulated galaxies are convolved with a PSF (obtained from the data) and are placed in empty areas of the observed H_{160} band image. We then run the procedure described above to extract surface brightness profiles and compare them to the input profiles.

A selection of these simulated profiles is shown in Figure 4.3. The input profiles are shown as solid black lines. The dashed grey lines indicate the two subcomponents of each simulated galaxy. The directly measured profiles are shown in green. The best-fit Sérsic models are shown in blue, and the residual-corrected profiles are shown in red. The residual-corrected profiles are plotted up to the radius where the uncertainty in the sky determination becomes significant. The effectiveness of the residual-correction method is clear: whereas a simple Sérsic fit in many cases under- or overpredicts the flux at $r > 5$ kpc, the residual-corrected profiles follow the input profiles extremely well up to the sky threshold (~ 10 kpc). The recovered flux within 10 kpc is on average 95% of the total input flux, with a 1-σ spread of 2%. Recovered effective radii are less accurate, as this quantity depends quite strongly on the extrapolation of the surface brightness profile to radii beyond 10 kpc. However, effective radii derived from the residual-corrected profiles are generally closer to the true effective radii than those derived from simple Sérsic fits.

4.4 MISSING FLUX IN COMPACT QUIESCENT Z $\sim$ 2 GALAXIES

We now use the residual-correction method to derive the surface brightness profiles of the $z \sim 2$ quiescent galaxies. The results are shown in Figures 4.4 and 4.4. The SEDs, shown in the top row, illustrate the low levels of UV and IR emission of the quiescent galaxies in our sample. Rest-frame color images are shown in the second row. These images indicate that the

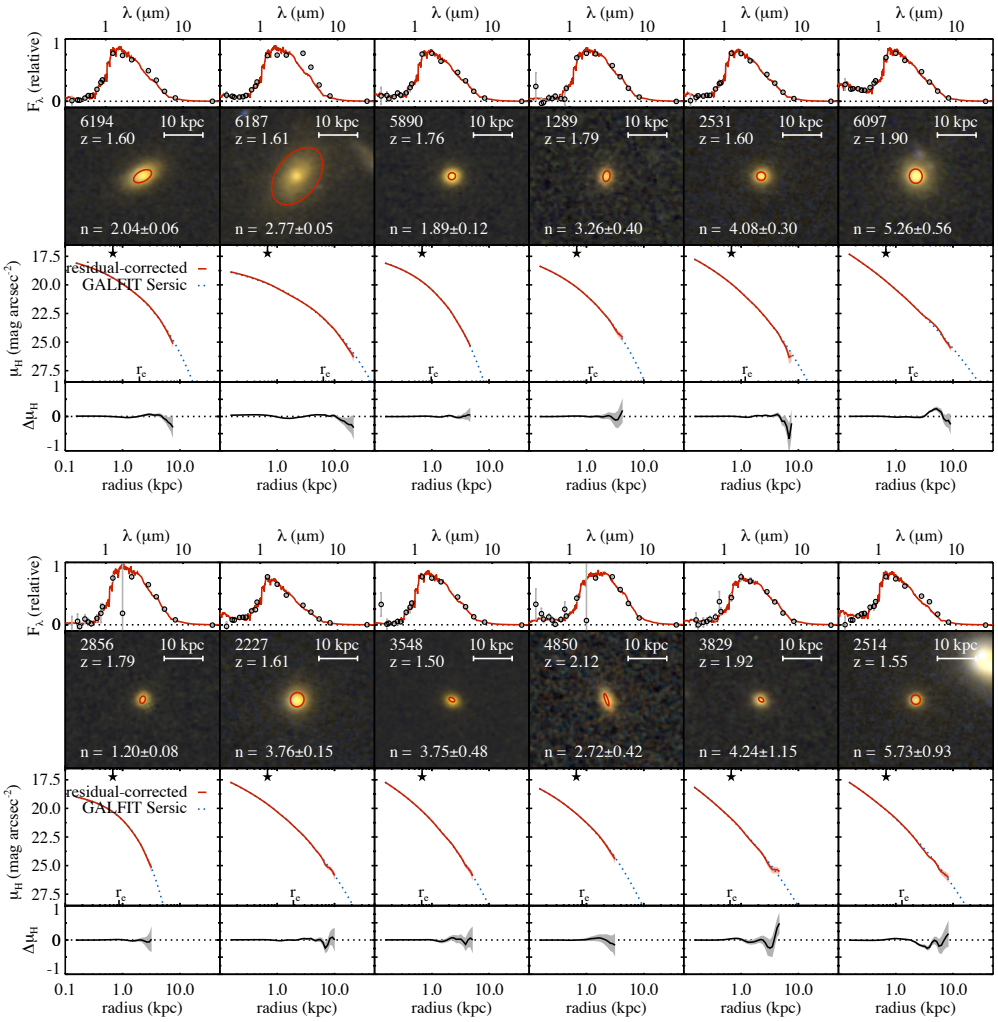

Figure 4.4: Broadband SEDs, color images and PSF-corrected surface brightness profiles of $z \sim 2$ quiescent galaxies. The SEDs, obtained with FAST (Kriek et al., 2009), are based on photometry from the FIREWORKS catalog. The color images are composed of rest-frame U_{336}, B_{438} and g_{475} images, obtained from the observed I_{814}, J_{125} and H_{160} data. The red ellipses are constructed from the best-fitting effective radii, axis ratios, and position angles. The best-fit Sérsic profiles, obtained using GALFIT, are indicated by blue dotted curves. Residual-corrected surface brightness profiles are shown in red. Effective radii and the PSF HWHM are indicated at the bottom and top axes, respectively. We are able to measure the true surface brightness profiles of these galaxies down to approximately 26 mag arcsec^{-2} and out to $r \approx 10$ kpc. In the bottom row we show the difference between the best-fit Sérsic profile and the residual-corrected profile. Individual residual-corrected profiles show deviations from simple Sérsic profiles, although these deviations are consistent with zero within the errors.

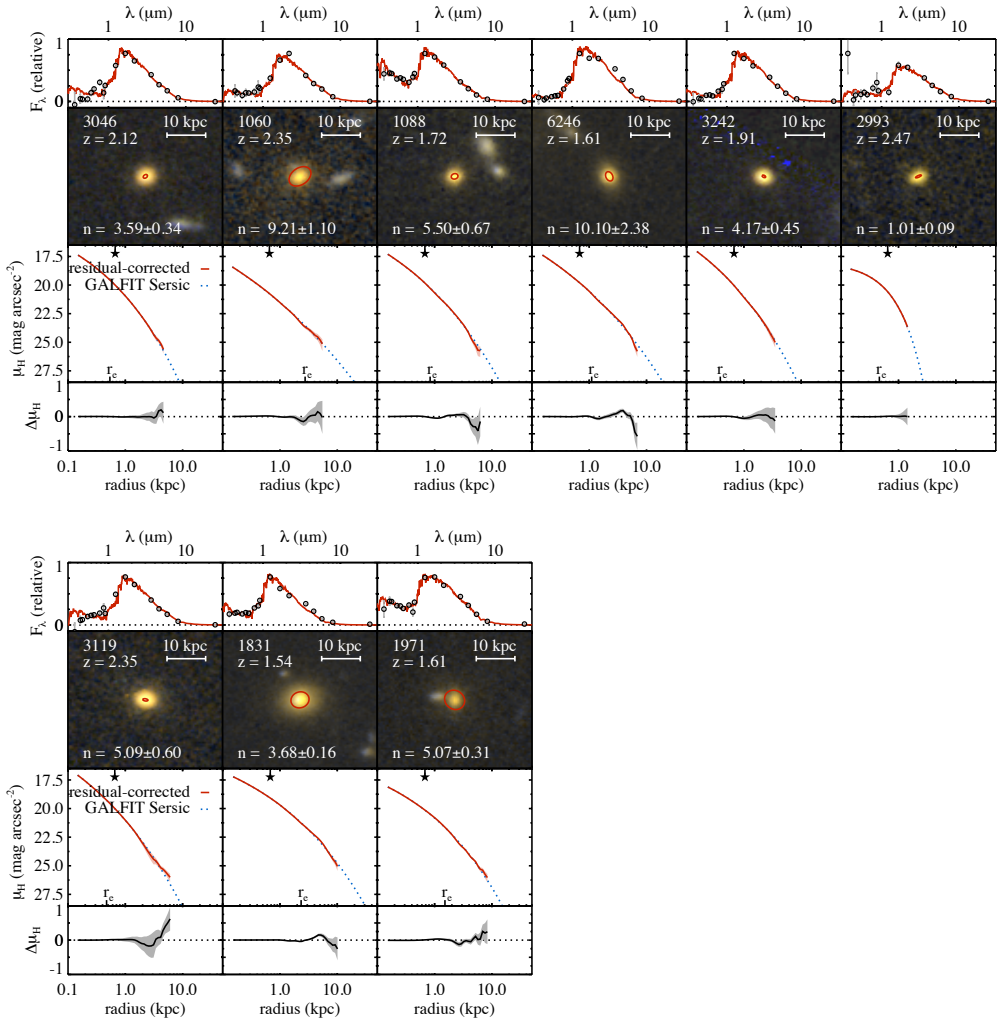

Figure 4.4: Continued.

galaxies in this sample generally have compact elliptical morphologies. Some galaxies have a nearby neighbor; in these cases we simultaneously fit both objects to account for possible contamination by flux from the companion object. In the third row, best-fit Sérsic profiles are shown in blue and residual-corrected profiles in red. The residual-corrected profiles follow the Sérsic profiles remarkably well. Most galaxies deviate slightly at large radii. The difference between the best-fit Sérsic profiles and the residual-corrected profiles are shown in the bottom row. The deviations are generally small within $2r_e$; for some galaxies larger deviations occur at larger radii, but in these cases the uncertainty is very high due to the uncertain sky. Overall, the profiles are consistent with simple Sérsic profiles. The profiles are given in Table 4.2, and can also be downloaded from `http://www.strw.leidenuniv.nl/~szomoru/`

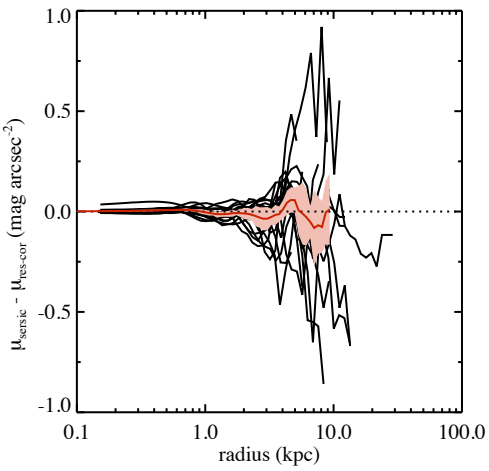

Figure 4.5: Deviations of galaxy profiles from Sérsic profiles. The difference between the best-fit Sérsic profile and the residual-corrected profile is plotted as a function of radius for all galaxies in our sample (black lines). The mean profile is shown in red, with the shaded light red region indicating the $1-\sigma$ spread in the distribution. Although individual galaxy profiles deviate from Sérsic profiles, on average the difference is consistent with zero.

In order to investigate whether the profiles of $z\sim2$ quiescent galaxies deviate systematically from Sérsic profiles we plot the difference between the best-fit Sérsic profile and the residual-corrected flux profile in Figure 4.5, for all galaxies. Black lines indicate the deviation profiles of individual galaxies, and their mean is indicated by the red line. The light red area shows the 1-σ spread around the mean. The mean profile is consistent with zero at all radii; the surface brightness profiles of quiescent galaxies at $z\sim2$ seem to be well described by Sérsic profiles. On average the residual correction increases or decreases the total flux of each galaxy in our sample by only a few percent, with an upper limit of 7%. The mean contribution of the residual flux to the total flux for all galaxies in our sample is -0.7%. Thus, we do not find evidence that indicates that there is missing low surface brightness emission around compact quiescent $z\sim2$ galaxies, and we therefore conclude that the small sizes found for these galaxies are correct.

4.5 THE MASS GROWTH OF Z $\sim$ 2 QUIESCENT GALAXIES

In the previous Section we have shown that the surface brightness profiles of $z\sim2$ quiescent galaxies closely follow Sérsic profiles, and that their sizes are not systematically underestimated due to a lack of sensitivity. We now compare their size distribution and surface

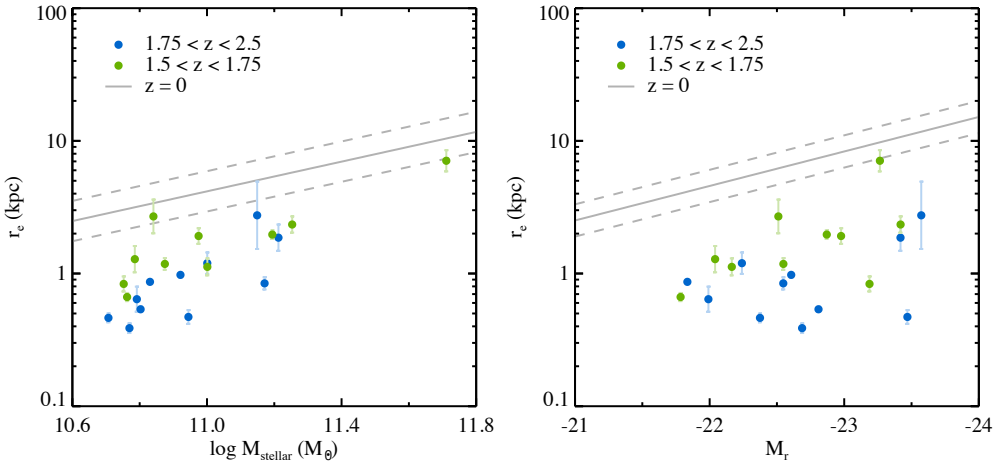

Figure 4.6: Relations between size and stellar mass (left panel) and size and rest-frame r-band absolute magnitude (right panel). Grey lines indicate the low-redshift mass-size and magnitude-size relations from Shen et al. (2003), green and blue points indicate the $z \sim 2$ sample (divided into low and high redshift bins, respectively). The $z \sim 2$ galaxies are, on average, almost an order of magnitude smaller than low-redshift galaxies of similar mass and luminosity. However, there is a significant range in sizes at both redshifts. The largest $z \sim 2$ galaxies lie very close to the $z = 0$ mass-size relation.

brightness profiles to those of low-redshift galaxies. In Figure 4.6 we show the mass-size and magnitude-size relations for the $z \sim 2$ galaxies and for low-redshift massive elliptical galaxies, taken from Shen et al. (2003). The $z \sim 2$ sample has been split into two redshift bins: $1.75 < z < 2.5$ and $1.5 < z < 1.75$ (shown in blue and green, respectively). The low-redshift sample is shown in grey. Galaxies at $z \sim 2$ are significantly smaller than those at $z = 0$. We fit a power law of the form $r_e \propto (1+z)^{\alpha}$ and find $\alpha = -0.94 \pm 0.16$, which is comparable to e.g., van der Wel et al. (2008) and van de Sande et al. (2011), but slightly steeper than Newman et al. (2010) and significantly shallower than Buitrago et al. (2008).

However, the $z \sim 2$ galaxies span a large range in size; some are supercompact, while others are as large as $z = 0$ galaxies. Following Shen et al. (2003), we quantify this range using $\sigma_{\log_{10} r_e}$, which is defined as the 1-σ spread in $\log_{10} r_e$ around the median mass-size relation, which we fix to the $z = 0$ slope. Note that we define the scatter in $\log_{10}$ basis, not the natural logarithm as used by Shen et al. (2003). It is equal to 0.24 ± 0.06 for our entire sample, while Shen et al. (2003) find values around $\sigma_{\log_{10} r_e} = 0.16$ for early-type galaxies at $z = 0.1$ in the same mass range. The values for the two high-redshift subsamples are 0.21 ± 0.11 at $1.5 < z < 1.75$ and 0.19 ± 0.07 at $1.75 < z < 2.5$. These values are upper limits, since they include the errors on individual size measurements; however, if our error estimates are correct, their effect on the scatter is $\lesssim 0.01$ dex. The scatter we measure is comparable to that found in **?**. These authors find $\sigma_{\log_{10} r_e} \approx 0.25$ for galaxies with $10^{10.7} M_{\odot} < M_{stellar} \lesssim 10^{11.7} M_{\odot}$ at $z \sim 2$. We note that our sample contains

several galaxies that are part of an overdensity at $z = 1.6$ (e.g., Gilli et al. 2003; Castellano et al. 2007; Kurk et al. 2009). In particular, the two largest galaxies in our sample are part of this overdensity. Excluding the $z = 1.6$ galaxies from our analysis does not significantly alter the spread in galaxy sizes in the $1.5 < z < 1.75$ redshift bin: $\sigma_{\log_{10} r_e} = 0.21 \pm 0.14$.

The size measurements used in Shen et al. (2003) have been shown to suffer from systematic errors due to background oversubtraction (Guo et al., 2009). As a result of this, the mass-size relation measured by Shen et al. (2003) is significantly shallower than that found by, e.g., Guo et al. (2009). We therefore repeat our determination of the scatter around the $z \sim 2$ mass-size relation using the Guo et al. (2009) measurements. This results in a decrease in the scatter by only ~ 0.03 dex, and does not affect our conclusions.

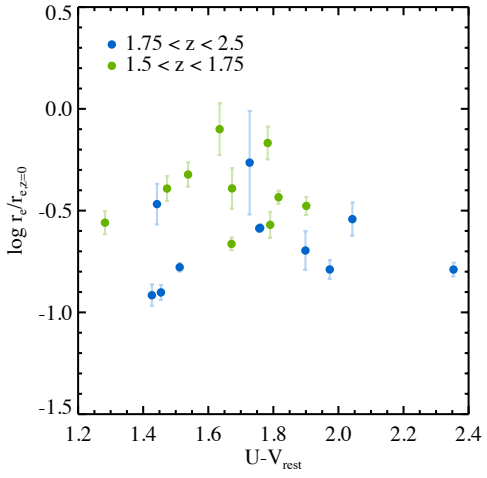

Figure 4.7: Offset from the $z = 0$ mass-size relation as a function of rest-frame $U - V$ color for galaxies at $1.5 < z < 1.75$ (green points) and $1.75 < z < 2.5$ (blue points). The offset is calculated by dividing the effective radius of each galaxy by the median effective radius of $z = 0$ quiescent galaxies with the same mass, using the $z = 0$ mass-size relation from Shen et al. (2003). The galaxies are split into two redshift bins. Assuming that rest-frame $U - V$ color is a good proxy for the mean stellar age of galaxies, we find no evidence for a correlation between galaxy compactness and galaxy age for $z \sim 2$ quiescent galaxies.

We note that, even within the limited redshift range under consideration, differences in redshift play a role: the galaxies in the $1.75 < z < 2.5$ subsample are clearly smaller than the $1.5 < z < 1.75$ galaxies. This may explain some of the disagreement between studies of high-redshift quiescent galaxies. In particular, the large effective radii found by Mancini et al. (2010) for some high-redshift quiescent galaxies could be due to the fact that they select galaxies with $1.4 < z < 1.75$. In this context, part of the size evolution between $z \sim 2$ and $z = 0$ could be due to the appearance of young, relatively large quiescent galaxies after $z \sim 2$ (e.g., van Dokkum et al. 2008; Franx et al. 2008; Saracco et al. 2009; van der Wel et al. 2009; Cassata et al. 2011). We note that Saracco et al. (2009) find evidence for a correlation of galaxy compactness with stellar age, such that the most compact high-redshift quiescent galaxies contain older stellar populations than quiescent galaxies that lie close to the $z = 0$ mass-size relation. We investigate this correlation in Figure 4.7, using rest-frame $U-V$ color as a proxy for galaxy age. We define galaxy compactness as the offset between the $z \sim 2$ galaxy sizes and the $z = 0$ mass-size relation of Shen et al. (2003): $r_e/r_{e,z=0} = r_e/(2.88 \times 10^{-6} \times M^{0.56})$. We find no evidence for a correlation between galaxy compactness and galaxy age in our data.

In Figure 4.8 we compare the stellar mass surface density profiles of the $z \sim 2$ galaxies to those of low redshift galaxies. Based on their masses and number densities, we expect $z \sim 2$ quiescent galaxies to evolve into the most massive low-redshift galaxies (e.g., van Dokkum et al. 2010). As a comparison sample we therefore use surface brightness profiles of elliptical galaxies with equal or higher mass in the Virgo cluster from Kormendy et al. (2009). These authors used a combination of space-based and ground-based observations to obtain surface brightness profiles with very high resolution and dynamic range, covering almost three orders of magnitude in radius. The surface brightness profiles have been converted to stellar mass surface density profiles using the total stellar mass-to-light ratios. We have ignored radial color gradients, which are known to exist at low and high redshift (e.g., van Dokkum et al. (2010); Szomoru et al. (2011); Guo et al. (2011)). These profiles are shown in grey, with the profiles of the $z \sim 2$ galaxies overplotted in blue and green.

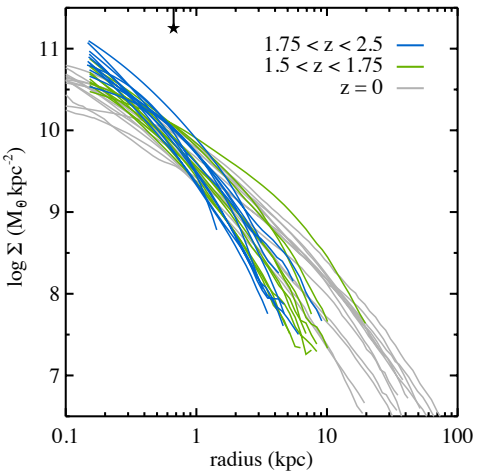

Figure 4.8: Comparison of stellar mass surface density profiles of $z \sim 2$ galaxies (blue and green curves) to elliptical galaxies in the Virgo cluster (Kormendy et al. 2009; grey curves). The Virgo galaxies are selected to have masses equal to or higher than those of the high-redshift galaxies. Radial color gradients are ignored when calculating the mass density profiles. The star, top left, indicates the PSF HWHM at $z = 2$. The central densities of the $z \sim 2$ galaxies are very similar to those of the $z = 0$ galaxies. At larger radii, however, significant evolution must occur if the $z \sim 2$ galaxies are to evolve into massive low-redshift elliptical galaxies.

What is most apparent in Figure 4.8 is that the central ($r < 1 - 3$ kpc) surface densities of the $z \sim 2$ galaxies are very similar to those of the $z = 0$ galaxies, while at larger physical radii (in kpc) the high-redshift galaxies have lower surface densities than the low-redshift galaxies. The profiles are in close agreement with previous studies (e.g., Bezanson et al. 2009; Carrasco et al. 2010). We compare the change in radial mass density profiles to the mass evolution of quiescent galaxies described in Brammer et al. (2011). These authors show that galaxies with a number density of 10^{-4} Mpc^{-3} have grown in mass by a factor ~ 2 since $z = 2$. As mentioned above, the mass contained within 3 kpc changes very little from $z \sim 2$ to $z = 0$; we find an increase on the order of 10%. However, the mass contained outside 3 kpc is approximately ten times higher for the $z = 0$ galaxies than for the $z \sim 2$ galaxies, and is equal to 58% of their total mass. Thus, slightly more than half of the total mass of the $z = 0$ ellipticals is located at $r > 3$ kpc, whereas the $z \sim 2$ galaxies contain nearly no mass at these radii. This is consistent with the Brammer et al. (2011) result, and suggests that compact $z \sim 2$ quiescent galaxies may survive intact as the cores of present-day massive ellipticals, with the bulk of

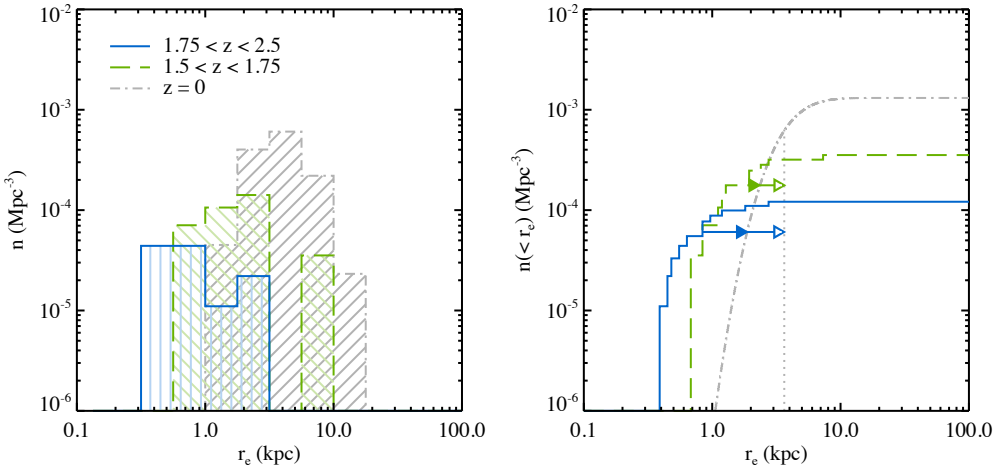

Figure 4.9: Comoving number density (left panel) and cumulative comoving number density (right panel) as a function of effective radius r_e, for galaxies at $1.75 < z < 2.5$, $1.5 < z < 1.75$, and $z = 0$ (solid blue, dashed green, and dot-dashed grey lines, respectively). The $z = 0$ number densities are obtained by combining the stellar mass function of Bell et al. (2003) with the mass-size relation of Shen et al. (2003). The $z \sim 2$ number densities have been scaled such that the total number density corresponds to the results of Brammer et al. (2011). Both the median effective radius and the total number density of quiescent galaxies show a strong increase from $z \sim 2$ to $z = 0$. The solid arrows in the right-hand panel indicate the minimum size growth required for high-redshift galaxies to grow into the smallest galaxies at $z = 0$. The open arrows indicate the size growth required for high-redshift galaxies to grow to the same median size as galaxies at $z = 0$. The minimum size growth required for $z \sim 2$ quiescent galaxies is approximately a factor 2 smaller than the median size growth between $z \sim 2$ and $z = 0$.

mass accretion since $z \sim 2$ occuring at large radii. This is consistent with an inside-out scenario of galaxy growth, as described in e.g., van Dokkum et al. (2010). We note that this discussion ignores transformations of star forming galaxies to the quiescent population.

Finally, we compare the comoving number densities and comoving cumulative number densities of our $z \sim 2$ sample to the number densities of $z = 0$ galaxies in Figure 4.9. To obtain the $z = 0$ number densities we combine the $z = 0$ mass function for early-type galaxies from Bell et al. (2003) with the mass-size relation of Shen et al. (2003): we use the relations appropriate for early-type galaxies and evaluate over the mass range $5 \times 10^{10} M_{\odot} < M_{stellar} < 5 \times 10^{11} M_{\odot}$. Given our small field size we cannot determine number densities accurately. We therefore adopt the number densities measured by Brammer et al. (2011). These authors used data covering a much larger field of view (approximately 25 times larger than the CANDELS GOODS-South field), and as such their results are less sensitive to cosmic variance. We scale our (cumulative) number density distributions such that the total number density corresponds to the Brammer et al. (2011) results. We note that our measured number densities are approximately a factor 2 smaller than those in Brammer et al. (2011), consistent with expectations from field-to-field varia-

tions (Somerville et al., 2004). We first consider the comoving number density distributions, plotted in the left panel of Figure 4.9. As expected, the median radius and the total number density increase with time, as existing galaxies grow in size and new quiescent galaxies appear. $r_{e,median} = 0.84 \pm 0.20$ kpc, 1.92 ± 0.45 kpc, and 3.82 ± 0.03 kpc at $1.75 < z < 2.5$, $1.5 < z < 1.75$ and $z = 0$, respectively.

We can place constraints on the minimum size growth of $z \sim 2$ galaxies by considering comoving cumulative number densities, shown in the right-hand panel of Figure 4.9. We assume that the population of $z \sim 2$ quiescent galaxies grows just enough to fall within the $z = 0$ size distribution, but doesn't necessarily grow to the same median size as $z = 0$. This results in a shift of the $z \sim 2$ cumulative number density distribution, indicated by the filled arrows in Figure 4.9. This shift is approximately a factor ~ 2 smaller than the size growth required for the $z \sim 2$ quiescent galaxy population to match the median size at $z = 0$ (indicated by the open arrows). Thus, in this minimal-growth scenario, half of the observed size evolution between $z \sim 2$ and $z = 0$ is due to the growth of existing galaxies, while the other half results from the appearance of new, larger quiescent galaxies at intermediate redshifts. These results are consistent with e.g., Cassata et al. (2011) and **?**.

4.6 SUMMARY AND CONCLUSIONS

In this Paper we have demonstrated that the small measured sizes of $z \sim 2$ massive quiescent galaxies are not caused by a lack of sensitivity to low surface brightness flux. Using deep data and a method which is sensitive to excess emission at large radii, we have shown that the surface brightness profiles of these galaxies are well described by Sérsic profiles. The median Sérsic index is $n_{median} = 3.7$, similar to low-redshift quiescent galaxies.

The sizes of $z \sim 2$ quiescent galaxies span a large range; although the median effective radius is small ($r_{e,median} = 1.1$ kpc), values up to ~ 7 kpc are observed. The scatter in $\log r_e$ is 0.24 at $z \sim 2$, aproximately 1.5 times as large as at $z = 0$. This indicates that the ``dead'' population of galaxies is very diverse at $z \sim 2$. We note that the size evolution between $z = 1.5$ and $z = 2.5$ is significant, which suggests that the cause of discrepancies in the results of different studies of the measured sizes of quiescent galaxies around $z = 2$ could be due to small differences in the redshift ranges considered.

Additionally, we have compared the stellar mass surface density profiles of $z \sim 2$ galaxies to those of massive early-type galaxies in the Virgo cluster. Although the densities within ~ 1 kpc are comparable, at larger radii the $z \sim 2$ galaxies show a clear deficit of mass. This puts strong constraints on models of galaxy formation and evolution. Firstly, most of the size buildup of $z \sim 2$ quiescent galaxies must occur at large radii (> 1 kpc). Secondly, a significant contribution from major gas-rich mergers since $z \sim 2$ seems to be ruled out, as this would disturb the inner density profiles of these galaxies. Minor, dry merging and slow accretion of matter seems to be the most viable method of evolving these galaxies into their $z = 0$ descendants.

Finally, we have investigated the evolution in the size distribution of massive quies-

cent galaxies. We conclude that the median size of massive quiescent galaxies changes by a factor ~ 4 between $z \sim 2$ and $z = 0$, and is accompanied by an increase in number density of a factor ~ 7. However, it is important to note that the size growth of individual galaxies is likely to be significantly smaller. The minimum required size growth for the $z \sim 2$ quiescent galaxy population is approximately a factor ~ 2 smaller than the median overall size growth. In this scenario the stronger overall size growth may be caused by the appearance of new, larger quiescent galaxies at intermediate redshifts.

One of the main observational uncertainties pertaining to the size evolution of massive quiescent galaxies now appears to be resolved; robust sizes, measured at high resolution and using very deep rest-frame optical data, indicate that galaxies at $z \sim 2$ were significantly smaller than equally massive galaxies at $z = 0$. However, the mechanisms driving this evolution and their precise effects on the structure of individual galaxies, as well as on the characteristics of the population as a whole, are still not entirely understood. Most studies seem to point towards gas-poor galaxy merging as the dominant growth process (e.g., Bezanson et al. 2009; Naab et al. 2009; Hopkins et al. 2010); however, it is unclear whether this can account for all the observed size growth. A complicating factor in such studies is that tracing the same group of galaxies across cosmic time is very difficult, since their masses, sizes and stellar population properties are not constant; selecting the same population of galaxies at different epochs is therefore not trivial. Studies at fixed (cumulative) number density may provide a solution to this problem, though only for relatively massive galaxies.

REFERENCES

Bell, E. F., McIntosh, D. H., Katz, N., & Weinberg, M. D. 2003, ApJS, 149, 289
Bezanson, R., van Dokkum, P. G., Tal, T., Marchesini, D., Kriek, M., Franx, M., & Coppi, P. 2009, ApJ, 697, 1290
Bezanson, R., et al. 2011, ApJ, 737, L31
Brammer, G. B., van Dokkum, P. G., & Coppi, P. 2008, ApJ, 686, 1503
Brammer, G. B., Whitaker, K. E., van Dokkum, P. G., et al. 2011, ApJ, 739, 24
Bruzual, G., & Charlot, S. 2003, MNRAS, 344, 1000
Buitrago, F., Trujillo, I., Conselice, C. J., et al. 2008, ApJ, 687, L61
Caon, N., Capaccioli, M., & D'Onofrio, M. 1993, MNRAS, 265, 1013
Cappellari, M., et al. 2009, ApJ, 704, L34
Carrasco, E. R., Conselice, C. J., & Trujillo, I. 2010, MNRAS, 405, 2253
Cassata, P., et al. 2010, ApJ, 714, L79
Cassata, P., Giavalisco, M., Guo, Y., et al. 2011, ApJ, 743, 96
Castellano, M., Salimbeni, S., Trevese, D., et al. 2007, ApJ, 671, 1497
Cenarro, A. J., & Trujillo, I. 2009, ApJ, 696, L43
Conroy, C., Gunn, J. E., & White, M. 2009, ApJ, 699, 486
Côté, P., Ferrarese, L., Jordán, A., et al. 2007, ApJ, 671, 1456, ApJ, 699, 486
Daddi, E., et al. 2005, ApJ, 626, 680
Damjanov, I., et al. 2009, ApJ, 695, 101
Ferrarese, L., Côté, P., Jordán, A., et al. 2006, ApJS, 164, 334
Förster Schreiber, N. M., Shapley, A. E., Erb, D. K., et al. 2011, ApJ, 731, 65
Förster Schreiber, N. M., Shapley, A. E., Genzel, R., et al. 2011, ApJ, 739, 45
Franx, M., et al. 2003, ApJ, 587, L79
Franx, M., van Dokkum, P. G., Schreiber, N. M. F., et al. 2008, ApJ, 688, 770
Gilli, R., Cimatti, A., Daddi, E., et al. 2003, ApJ, 592, 721
Graham, A. W., Erwin, P., Trujillo, I., & Asensio Ramos, A. 2003, AJ, 125, 2951
Grogin, N. A., Kocevski, D. D., Faber, S. M., et al. 2011, ApJS, 197, 35
Guo, Y., McIntosh, D. H., Mo, H. J., et al. 2009, MNRAS, 398, 1129
Guo, Y., Giavalisco, M., Cassata, P., et al. 2011, ApJ, 735, 18
Hopkins, P. F., Bundy, K., Murray, N., Quataert, E., Lauer, T. R., & Ma, C.-P. 2009, MNRAS, 398, 898
Hopkins, P. F., Croton, D., Bundy, K., et al. 2010, ApJ, 724, 915
Koekemoer, A. M., Faber, S. M., Ferguson, H. C., et al. 2011, ApJS, 197, 36
Kormendy, J., Fisher, D. B., Cornell, M. E., & Bender, R. 2009, ApJS, 182, 216
Kriek, M., et al. 2006, ApJ, 649, L71
Kriek, M., van Dokkum, P. G., Labbé, I., et al. 2009, ApJ, 700, 221
Kroupa, P. 2001, MNRAS, 322, 231
Kurk, J., Cimatti, A., Zamorani, G., et al. 2009, A&A, 504, 331
Mancini, C., et al. 2010, MNRAS, 401, 933
Martinez-Manso, J., Guzman, R., Barro, G., et al. 2011, ApJ, 738, L22

Muzzin, A., van Dokkum, P., Franx, M., et al. 2009, ApJ, 706, L188
Naab, T., Johansson, P. H., & Ostriker, J. P. 2009, ApJ, 699, L178
Newman, A. B., Ellis, R. S., Treu, T., & Bundy, K. 2010, ApJ, 717, L103
Newman, A. B., Ellis, R. S., Bundy, K., & Treu, T. 2012, ApJ, 746, 162
Onodera, M., et al. 2010, ApJ, 715, L6
Oser, L., Naab, T., Ostriker, J. P., & Johansson, P. H. 2012, ApJ, 744, 63
Patel, S. G., Holden, B. P., Kelson, D. D., et al. 2011, arXiv:1107.3147
Peng, C. Y., Ho, L. C., Impey, C. D., & Rix, H.-W. 2002, AJ, 124, 266
Saracco, P., Longhetti, M., & Andreon, S. 2009, MNRAS, 392, 718
Sérsic, J. L. 1968, Atlas de galaxias australes (Cordoba, Argentina: Observatorio Astronomico, 1968)
Shen, S., Mo, H. J., White, S. D. M., et al. 2003, MNRAS, 343, 978
Somerville, R. S., Lee, K., Ferguson, H. C., et al. 2004, ApJ, 600, L171
Szomoru, D., et al. 2010, ApJ, 714, L244
Szomoru, D., Franx, M., Bouwens, R. J., et al. 2011, ApJ, 735, L22
Toft, S., et al. 2007, ApJ, 671, 285
Taylor, E. N., Franx, M., Glazebrook, K., et al. 2010, ApJ, 720, 723
Taylor, E. N., Franx, M., Brinchmann, J., van der Wel, A., & van Dokkum, P. G. 2010, ApJ, 722, 1
Trujillo, I., Erwin, P., Asensio Ramos, A., & Graham, A. W. 2004, AJ, 127, 1917
Trujillo, I., et al. 2006, MNRAS, 373, L36
Trujillo, I., Cenarro, A. J., de Lorenzo-Cáceres, A., et al. 2009, ApJ, 692, L118
van der Wel, A., Holden, B. P., Zirm, A. W., Franx, M., Rettura, A., Illingworth, G. D., & Ford, H. C. 2008, ApJ, 688, 48
van der Wel, A., Bell, E. F., van den Bosch, F. C., Gallazzi, A., & Rix, H.-W. 2009, ApJ, 698, 1232
van de Sande, J., et al. 2011, ApJ, 736, L9
van Dokkum, P. G., et al. 2008, ApJ, 677, L5
van Dokkum, P. G., Kriek, M., & Franx, M. 2009, Nature, 460, 717
van Dokkum, P. G., et al. 2010, ApJ, 709, 1018
Williams, R. J., Quadri, R. F., Franx, M., van Dokkum, P., & Labbé, I. 2009, ApJ, 691, 1879
Wuyts, S., Labbé, I., Schreiber, N. M. F., Franx, M., Rudnick, G., Brammer, G. B., & van Dokkum, P. G. 2008, ApJ, 682, 985
Wuyts, S., Franx, M., Cox, T. J., et al. 2009, ApJ, 700, 799
Wuyts, S., Cox, T. J., Hayward, C. C., et al. 2010, ApJ, 722, 1666